ACS NANO

www.acsnano.org

Article

Low-Self-Discharge Nanoconfined Hydrogel Electrolyte for Stable High-Energy-Density Aqueous Zinc–Iodine Batteries

Renming Liu, Dongdong Wang,* Ze Gao, Daming Yang, Yuying Li, Xintao Long, Dan Luo,* Ming Feng,* and Zhongwei Chen*

Cite This: *ACS Nano* 2026, 20, 5217–5227

Read Online

ACCESS | Metrics & More | Article Recommendations | Supporting Information

ABSTRACT: Aqueous zinc–iodine batteries (AZIBs) leveraging four-electron $I^-/I^0/I^+$ redox chemistry show great promise in safe energy storage systems. However, realizing Ah-level AZIBs with industrial-grade parameters (≥10 mg cm^{-2} mass loading) remains fundamentally challenging. Here, we prepare the hydrogel electrolyte with mesoporous nanoparticles SBA-15 (MNPHE) by a nanoconfined polymerization strategy. The framework confinement effect, anion confinement effect, and free water confinement effect are achieved through Lewis acid–base interactions and hydrogen bond networks. The multiconfinement effects yield simultaneous ultrahigh mechanical strength (501 kPa tensile strength) and a record-high Zn^{2+} transference number ($t_{Zn^{2+}}$ = 0.95), which collectively suppressed polyiodide generation and I^+ species hydrolysis. This results in markedly enhanced reversibility and kinetics for four-electron $I^-/I^0/I^+$ redox chemistry under a high-I_2-mass-loading cathode. Based on MNPHE, the Zn||I_2 full cells display a record-low self-discharge rate with only 20% capacity loss after three months and a prolonged lifetime of 100,000 cycles at 25 C. Furthermore, Ah-level four-electron Zn||I_2 pouch cells achieve excellent cyclability of 800 cycles and an ultrahigh cathode-mass-specific energy density of 466.7 Wh kg^{-1}, surpassing all aqueous Zn-based systems in the Ah-level regime.

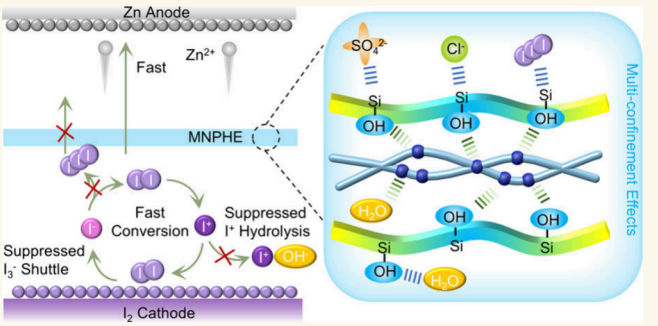

KEYWORDS: *zinc–iodine batteries, hydrogel electrolyte, self-discharge, Ah-level pouch cell, high energy density*

INTRODUCTION

Aqueous zinc metal batteries have garnered significant attention for large-scale energy storage due to their attractive attributes, including intrinsic safety, low cost, and high theoretical capacity.[1,2] The widely studied intercalation cathodes (e.g., layered metal oxides, Prussian blue analogues) suffer from fundamental limitations, such as sluggish Zn^{2+} insertion/extraction kinetics constrained by strong host–framework electrostatic interactions and progressive capacity decay from repeated structural distortion. The conversion-type cathodes (S, Se, Te, I_2, Br_2) circumvent these issues via multielectron redox mechanisms with accelerated kinetics.[3,4] Particularly, aqueous zinc–iodine batteries (AZIBs) demonstrate exceptional promise by leveraging earth-abundant iodine resources (~55 μg L^{-1} in seawater).[5,6] Offering both a higher redox potential (~1.8 V vs Zn^{2+}/Zn) and a greater theoretical capacity (422 mAh g^{-1}), these four-electron AZIBs surpass the performance of dominant Zn-MnO_2 systems.[7]

Despite these advantages, practical deployment of four-electron AZIBs faces major challenges, namely, the polyiodide shuttle effect during the I^-/I^0 conversion and water induced hydrolysis of I^+ species during the I^0/I^+ conversion, severely hindering the reversibility. Achieving highly reversible four-electron AZIBs necessitates the simultaneous suppression of both polyiodide shuttling and I^+ hydrolysis. Significant efforts have been devoted to suppressing polyiodide shuttle and I^+ hydrolysis in four-electron AZIBs through cathode host engineering,[8] catalytic mediators,[9,10] and electrolyte optimization.[11,12] Among these methods, electrolyte engineering involves the elaborative introduction of additives/cosolvents, hydrated eutectic electrolytes, and highly concentrated electrolytes shows distinct advantages for high-reversible four-electron $I^-/I^0/I^+$ redox chemistry. Qiao et al. reported hexamethylenetetramine (HMTA) as an electrolyte additive that effectively suppresses the polyiodide shuttle effect and enhances the stability of the I^+ species against hydrolysis, significantly enhancing the reversibility and cycling life of four-electron AZIBs.[13] He et al. developed a dynamical interface design strategy by introducing functional tetraethylammonium cations (TEA^+) into 15 m $ZnCl_2$ electrolytes. Electrically reinforced TEA^+ suppresses the migration of water molecules, creating a

Received: November 26, 2025
Revised: January 23, 2026
Accepted: January 23, 2026
Published: February 2, 2026

https://doi.org/10.1021/acsnano.5c20669
ACS Nano 2026, 20, 5217–5227

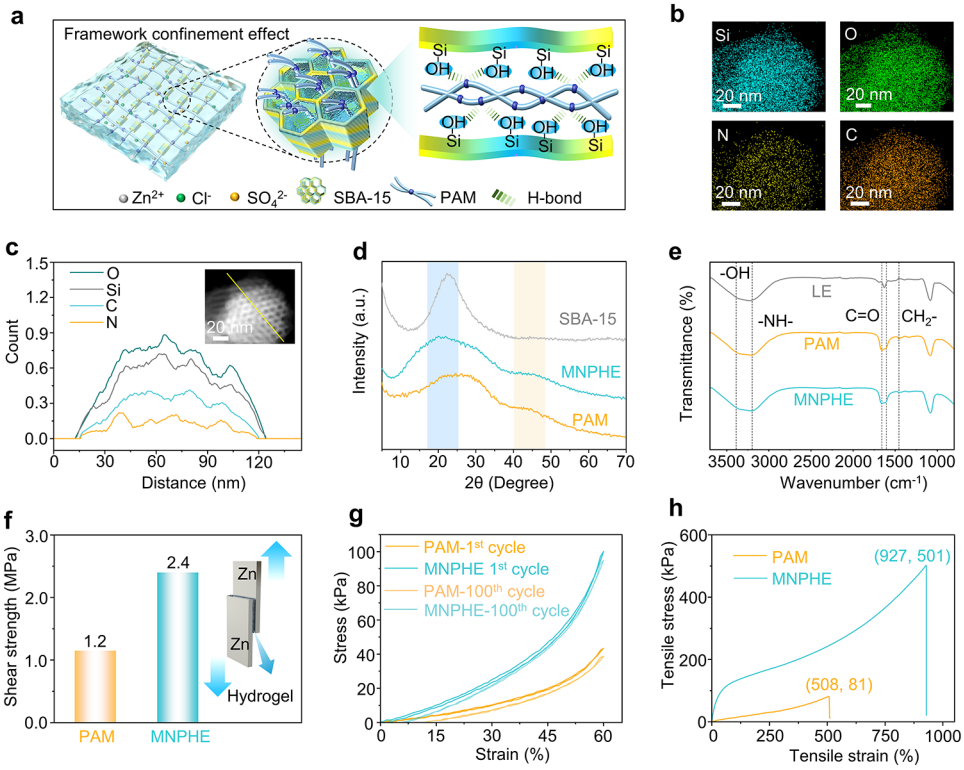

Figure 1. Physical properties of MNPHE prepared by a nanoconfined polymerization strategy. (a) Schematic illustrations of the MNPHE and framework confinement effects. (b) Corresponding element mapping of MNPHE. (c) EDX line-scanning profiles of MNPHE. (d) XRD patterns of SBA-15, PAM, and MNPHE. (e) FTIR spectra of LE, PAM, and MNPHE. (f) Shear strength between two Zn foils adhered with PAM and MNPHE. (g) Compressive stress−strain curves of PAM and MNPHE at 60% strain. (h) Tensile stress−stretch curves of PAM and MNPHE.

water-poor and Cl^--rich interface that improves reversibility of Zn stripping/plating behavior and four-electron iodine redox chemistry.[14] Despite these advancements, four-electron AZIBs still face some unresolved problems in the high-loading I_2 cathode (≥10 mg cm^{-2}) and Ah-level pouch cell architecture. The realization of long-cycle, Ah-level four-electron zinc−iodine pouch cells remains challenging.

Herein, we propose a nanoconfined polymerization strategy by introducing mesoporous nanoparticles SBA-15 as nanochannels to develop tough hydrogel electrolyte, achieving durable Ah-level four-electron zinc−iodine pouch cells with a thick cathode with practical mass loading (≥10 mg cm^{-2}). The MNPHE serves as proof of concept for this strategy, demonstrating strong hydrogen bonding interactions between SBA-15 and the interpenetrating polymer segments, which leads to effective immobilization of the polymer segments and enhanced mechanical strength (501 kPa tensile strength). Simultaneously, anion confinement effect promotes Zn^{2+} diffusion kinetics, achieving a record Zn^{2+} transfer number ($t_{Zn^{2+}}$ = 0.95), which enables uniform Zn plating/stripping. The confinement of free H_2O effectively suppresses polyiodide generation and I^+ species hydrolysis, leading to enhanced four-electron $I^-/I^0/I^+$ conversion kinetics and reversibility under a high mass loading of the I_2 cathode. As a result, the Zn||I_2 full cell exhibits remarkably low self-discharge, retaining 80% of its initial capacity after three months of open-circuit storage, along with a long cycling lifetime exceeding 100,000 cycles at a high rate of 25 C. Notably, an Ah-level Zn||I_2 pouch cell based on a four-electron transfer process demonstrates excellent cycling stability, operating steadily over 800 cycles. Its mass energy density, calculated based on the cathode active material, reaches up to 466.7 Wh kg^{-1}, setting a new record among reported Ah-level zinc-based energy storage devices. This work proposes a general design strategy for hydrogel electrolytes, offering a new route to high-energy-density zinc−iodine electrochemistry and paving the way for intrinsically safe grid-scale energy storage technologies.

RESULTS AND DISCUSSION

The SBA-15 as a representative of mesoporous nanoparticles is selected to investigate its effects on hydrogel properties. SBA-15 is a mesoporous nanoparticle consisting of silica with enriched silanol (Si−OH) groups (Figures S1 and S2) and exhibiting a two-dimensional hexagonal through-pore structure (Figure S3). The MNPHE was prepared through *in situ* polymerization of polyacrylamide within meso-channels of SBA-15, leading to a novel framework confinement effect (Figure 1a). In addition, to highlight the advantages of hydrogel electrolytes and the multiconfinement effects of the MNPHE, the liquid electrolyte (LE) and polyacrylamide hydrogel electrolyte (PAM) were used as control samples. Figure S4 provides a schematic illustration detailing the preparation process and components of the electrolytes. Transmission electron microscopy (TEM) and the corresponding energy dispersive X-ray (EDX) line scan analysis demonstrate that the C and N element is distributed within 15.7−119.5 nm, while Si and O elements span a wider range of 12.6−124.1 nm (Figure 1b,c). Such differentiation predominantly originates from confined polymerization within the meso-channels, leading to the more confined distribution of N and C compared to the framework elements (Si and O). Meanwhile, the pore size and specific surface area of SBA-15

https://doi.org/10.1021/acsnano.5c20669
ACS Nano 2026, 20, 5217−5227

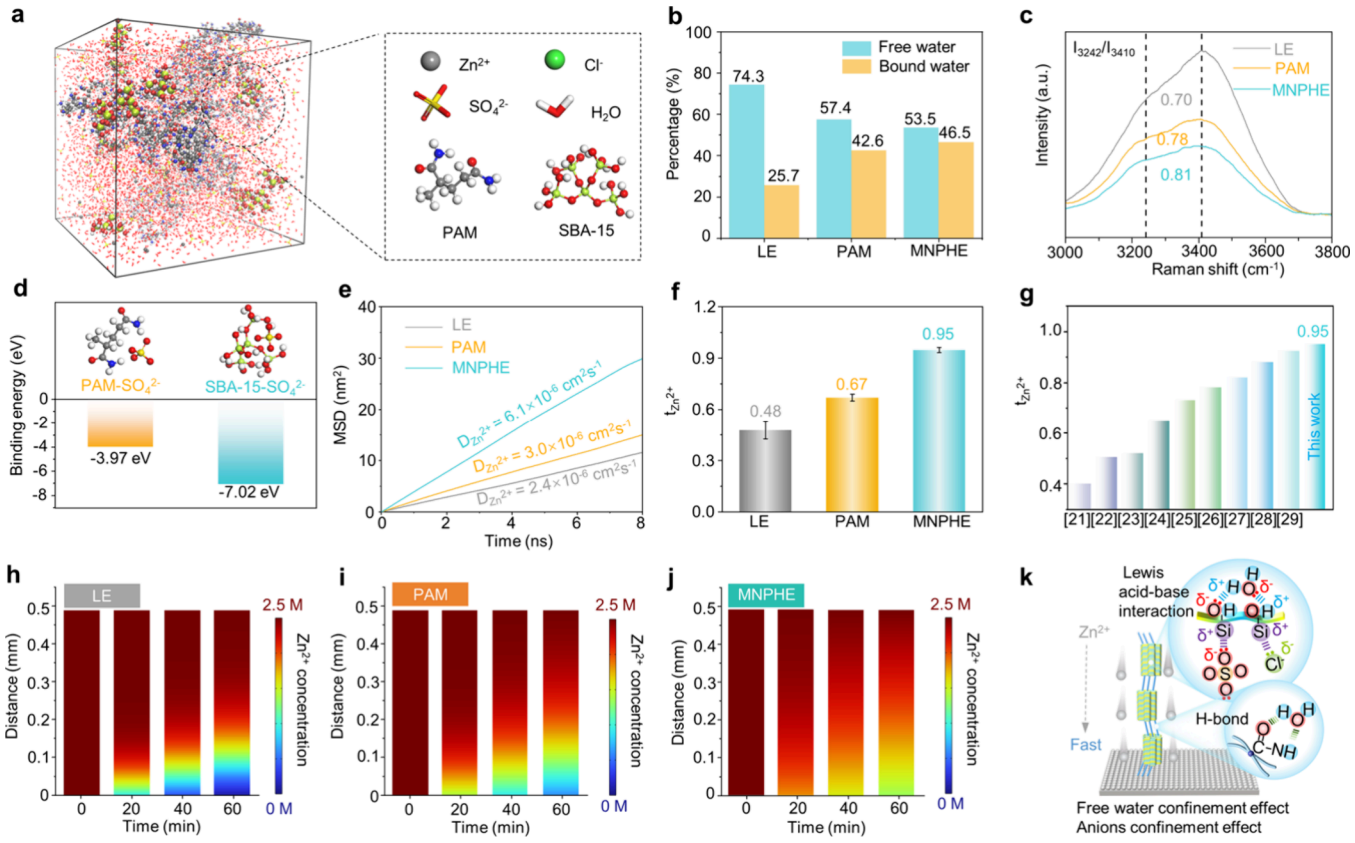

Figure 2. Enhanced reaction kinetics by anion confinement effect. (a) Molecular configuration of MNPHE by MD simulations. (b) The percentages of free water and bound water in different electrolytes. (c) Raman spectra of the O−H stretching in LE, PAM, and MNPHE. (d) Binding energies of PAM-SO_4^{2-} and SBA-15-SO_4^{2-}. (e) MSD of Zn^{2+} diffusion in different electrolytes. (f) $t_{Zn^{2+}}$ in LE, PAM, and MNPHE. (g) Comparison of $t_{Zn^{2+}}$ with the data reported in the literatures. The COMSOL simulation results of the Zn^{2+} concentration distribution in (h) LE, (i) PAM, and (j) MNPHE during the Zn plating process. (k) Schematic illustration of the free water confinement and anion confinement effect in MNPHE.

are reduced after polymerization, further confirming confined polymerization within the mesochannels (Figure S5). The fabricated MNPHE exhibits exceptional processability, enabling accurate tailoring into various geometries and dimensions to meet device-specific requirements. As shown in Figure S6, the MNPHE are precisely engineered to conform with coin and pouch cell specifications, with a thickness of 0.5 mm. PAM and MNPHE display broad XRD peaks at approximately 25° (Figure 1d), confirming their amorphous and noncrystalline nature (Figure 1d). Notably, the incorporation of SBA-15 induces a slight shift in the diffraction peaks of MNPHE compared to PAM and the diffraction peak of MNPHE is significantly broader than PAM, indicating a higher degree of structural disorder. This enhanced amorphous nature facilitates rapid Zn^{2+} ion migration within the MNPHE and endows it with superior mechanical flexibility during long-term cycling. Fourier transform infrared spectroscopy (FTIR) reveals strong absorption peaks at 1457, 1661, 1612.7, 3197.6, and 3365.1 cm^{-1}, which corresponds to the CH_2 in-plane shear, the amide I and II bands, N−H, and O−H stretching vibration of PAM, respectively (Figure 1e).[15,16] The FTIR bands of MNPHE and PAM remain identical, indicating that the hydrogel matrix network remains structurally unchanged. In addition, scanning electron microscopy (SEM) further revealed that the freeze-dried MNPHE possesses a porous microstructure, which is conducive to rapid ion diffusion (Figure S7).

The mechanical properties of PAM and MNPHE were measured by using a universal testing machine. Strikingly, the MNPHE exhibits exceptional interfacial bonding characteristics, achieving a remarkable shear strength of 2.4 MPa (Figures 1f and S8). In addition, the practical application of AZIBs necessitates exceptional mechanical durability in hydrogel electrolytes to withstand the cumulative stresses arising from recurrent Zn plating/stripping cycles. Remarkably, the compressive loading−unloading profiles demonstrate that MNPHE maintains exceptional structural integrity. After 100 compression cycles at 60% strain, its cyclic stress−strain curves and peak stress values show no significant changes compared to PAM, confirming the superior elasticity and elastic recovery properties of MNPHE (Figure 1g). Additionally, MNPHE demonstrates a 6.2-fold enhancement in tensile strength and elongation at break with a significant increase from 508% to 927% (Figures 1h and S9). High mechanical strength suppresses Zn dendrite growth, reducing internal short-circuit risk. The tensile strength of the hydrogel with SiO_2 nanoparticles is much lower than that of MNPHE (Figure S10), demonstrating the crucial role of framework confinement effects owing to the presence of a mesopore.

Although water as an electrolyte offers high safety and facilitates Zn^{2+} transport, free water can induce a series of parasitic reactions at both the cathode and anode of batteries.[17] To demonstrate the confinement effect of MNPHE on free water, we performed molecular dynamics (MD) simulations

https://doi.org/10.1021/acsnano.5c20669
ACS Nano 2026, 20, 5217−5227

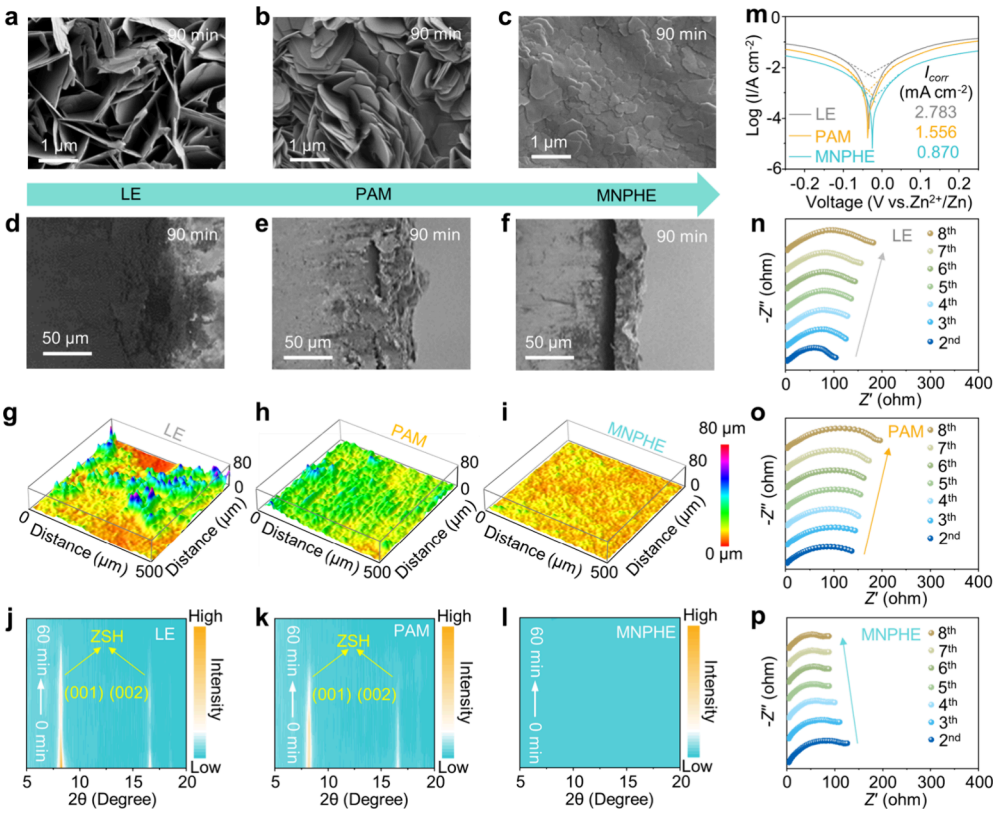

Figure 3. Growth behaviors of Zn anode and anticorrosion effect investigation in MNPHE. (a–f) Top-view and side-view SEM images and (g–i) LCSM images of the Zn anode after Zn deposition in different electrolytes. (j–l) *In situ* XRD patterns of the Zn anode during the deposition process at 10 mA cm^{-2}. (m) Tafel curves of Zn||Zn in different electrolytes. (n–p) *In situ* EIS curves of Zn||Zn cells with different electrolytes during continuous cycles.

(Figures 2a and S11–S13). Compared with LE and PAM, the proportion of bound water in MNPHE increases dramatically from 25.7% to 46.5%, which showed that the activity of water in MNPHE was reduced (Figure 2b and Table S1). Density functional theory (DFT) calculations revealed a higher binding energy for SBA-15-H_2O (−0.83 eV) than for H_2O-H_2O (−0.348 eV) or PAM-H_2O (−0.547 eV), indicating a strong binding affinity of MNPHE with water (Figure S14). In addition, the region between 3800 and 3000 cm^{-1} is further analyzed using Raman spectra to investigate the variation of hydrogen bonds in various electrolytes (Figure 2c). The Raman peaks at 3242 and 3410 cm^{-1} were assigned to symmetric and asymmetric O–H stretching vibrations of H_2O, respectively.[18,19] The ratio of intensities (I_{3242}/I_{3410}) represents the relative hydrogen-bond strength.[20] MNPHE exhibits an I_{3242}/I_{3410} ratio (0.81) higher than those of both PAM (0.78) and LE (0.7), indicating an interaction between Si–OH groups and water molecules. Meanwhile, the ^1H NMR spectra of MNPHE shows a more pronounced downfield shift compared to LE and PAM (Figure S15), resulting from its enhanced hydrogen bond networks.

Except for the confinement of free water, the confinement effect of anions in MNPHE was also investigated. As shown in Figures 2d and S16, the binding energies of SBA-15-SO_4^{2-} and SBA-15-Cl^- (−7.02 and −3.18 eV) are significantly higher than PAM-SO_4^{2-} and PAM-Cl^- (−3.97 and −2.19 eV), indicating the strong affinity of anions in MNPHE which thereby facilitates Zn^{2+} diffusion. Meanwhile, MSD analysis exhibits that the diffusion coefficient of Zn^{2+} in MNPHE (6.1×10^{-6} m^2 s^{-1}) is higher than that in LE (3×10^{-6} m^2 s^{-1}) and PAM (2.4×10^{-6} m^2 s^{-1}) (Figure 2e). The same results are also obtained by the coefficient of anions in MNPHE (Figure S17). Ionic conductivity was characterized by electrochemical impedance spectroscopy. The MNPHE electrolyte shows a high ionic conductivity, averaging 16.8 mS cm^{-1}. This value is comparable to that of LE (18.6 mS cm^{-1}) and is approximately twice that of the conventional PAM electrolyte (7.6 mS cm^{-1}) (Figure S18). The $t_{Zn^{2+}}$ was measured by the Bruce–Vincent method (Figure S19 and Table S2). As shown in Figure 2f, the $t_{Zn^{2+}}$ of MNPHE (0.95) is significantly higher than those of LE (0.48) and PAM (0.67). Notably, the MNPHE demonstrates a superior $t_{Zn^{2+}}$ that substantially exceeds the values reported in most existing hydrogel electrolytes (Figure 2g).[21−29] These results collectively demonstrate that the introduction of MNPHE successfully constructs fast Zn^{2+} migration pathways, ensuring a uniform ion flux distribution.

Finite-element method simulations of Zn^{2+} concentration and potential distributions induced by Zn^{2+} diffusion for different electrolytes were performed by COMSOL multi-physics software with 10 mA cm^{-2}. The LE shows rapid concentration gradients within 20 min, leading to complete interfacial depletion by 40 min (Figure 2h). While PAM exhibits similar but delayed gradient formation (Figure 2i). Remarkably, MNPHE maintains exceptional uniformity in both Zn^{2+} distribution and potential field throughout the 60 min operation (Figures 2j and S20), attributing to a fast Zn^{2+} diffusion kinetics. Figure S21 provides a mechanistic interpretation for the COMSOL simulation results. The slow diffusion of Zn^{2+} in LE and PAM hinders its timely supply to the Zn anode surface, leading to a severe concentration

https://doi.org/10.1021/acsnano.5c20669
ACS Nano 2026, 20, 5217−5227

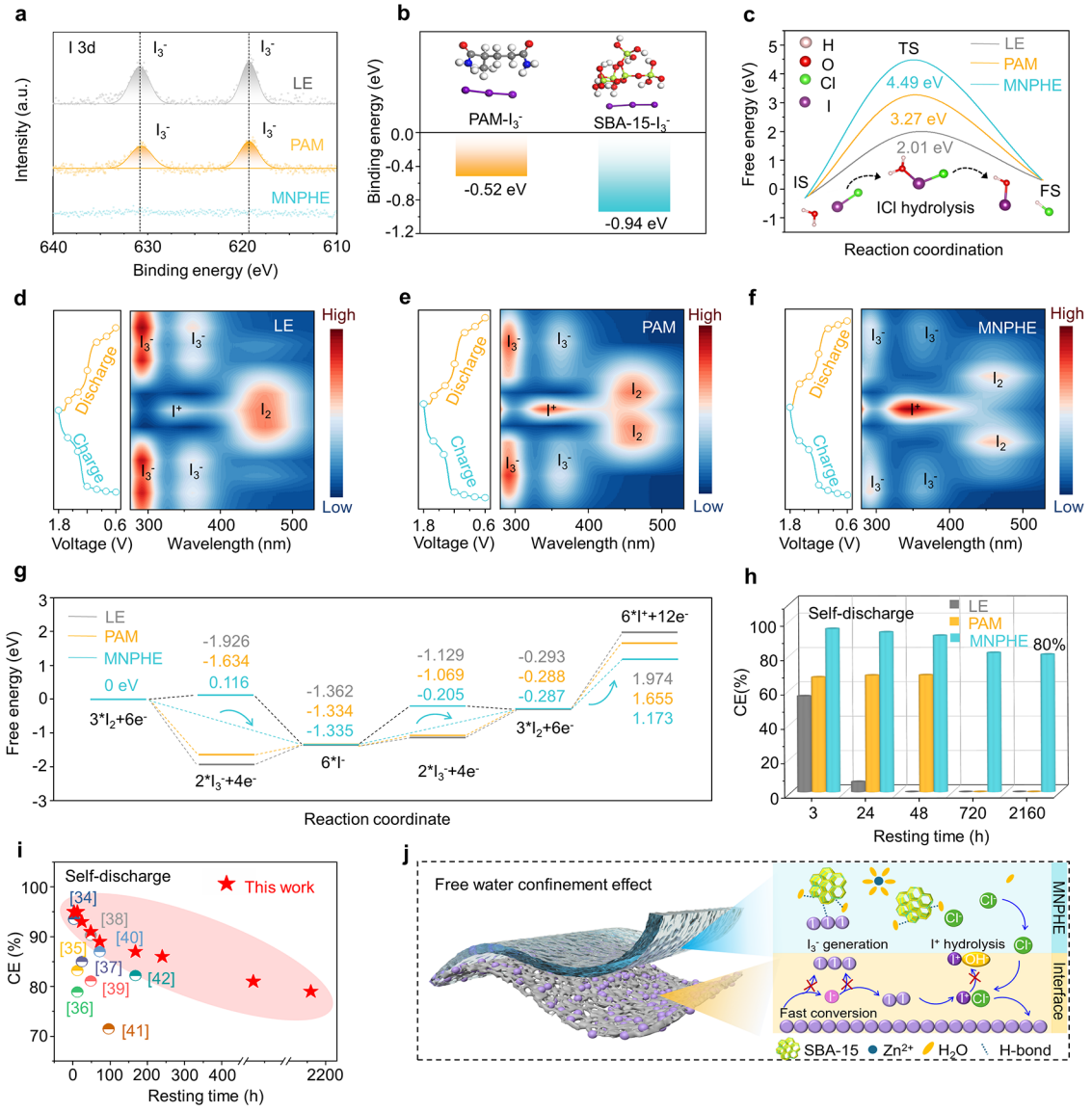

Figure 4. Suppression of polyiodides and the immobilization of I^+ species. (a) I 3d XPS spectra of the Zn anode surface after cycling. (b) The binding energy of I_3^- with PAM and SBA-15. (c) The hydrolysis reaction energy barriers of ICl in different electrolytes. (d–f) *Ex situ* UV–vis spectra of cathodes immersed in acetonitrile at different potentials. (g) Gibbs free energy of the I_2 reduction process in MNPHE. (h) Self-discharge performance of Zn||I_2 cells with LE, PAM, and MNPHE. (i) Comparison of the self-discharge performance of four-electron AZIBs in the published literature and this work. (j) Schematic illustration of the confinement effect of free H_2O in MNPHE.

gradient and the formation of a distinct space-charge layer, which promote Zn dendrite growth. In contrast, MNPHE facilitates rapid Zn^{2+} diffusion and enables uniform Zn^{2+} deposition. Based on the above theoretical calculations and experimental results, the underlying reasons can be analyzed as follows. In MNPHE, Lewis acid–base interactions between its functional groups (Si–O–Si and Si–OH) and SO_4^{2-}/H_2O restrict anion and water movement, thus enhancing Zn^{2+} transport. Meanwhile, the water activity can be further reduced through hydrogen bonding between water molecules and the polar amide groups (–$CONH_2$) on MNPHE polymer chains (Figure 2k).[30,31]

The growth behavior and corrosion resistance of the Zn anode are critically determined by the content of free water in the electrolyte and the Zn^{2+} diffusion rate. First, the chronoamperometry (CA) test proves that the rapid 2D diffusion of Zn^{2+} in LE leads to inhomogeneous Zn deposition. In contrast, the MNPHE exhibits the 3D diffusion process, leading to a stable and low current density, indicating that Zn nuclei evolved slowly to form uniform Zn deposition (Figure S22). The SEM and confocal laser scanning microscopy (CLSM) were used for direct observation of Zn deposition behavior on the anode in different electrolytes. The top-view SEM images display a large number of disordered nanosheet distributions in the LE (Figures 3a and S23), with this characteristic becoming increasingly distinct over the whole deposition process. The similar dendritic structures are also observed in the PAM (Figure 3b). Notably, the Zn anode in MNPHE maintains a flat surface without any observable protrusions (Figure 3c). Concurrently, the side-view SEM images show a porous and loose structure in LE and PAM after Zn deposition (Figure 3d,e). In contrast, the Zn deposition layer is compact and dense without dendrite formation in MNPHE (Figure 3f). The CLSM images reveal a flat and

https://doi.org/10.1021/acsnano.5c20669
ACS Nano 2026, 20, 5217–5227

compact morphology of the Zn anode within the MNPHE after deposition. On the contrary, the Zn anode within PAM and LE exhibits a rough surface with a multitude of protuberances (Figure 3g–i). All morphological results align with the electrochemical behavior and are discussed later.

Due to the electrolyte-induced corrosive effect, the Zn anode surface usually forms a large amount of irregularly shaped $Zn_4SO_4(OH)_6$ (ZSH) during operation processes of the battery. The accumulation of these deactivated ZSH induces uneven Zn stripping/plating, resulting in dendrite formation and battery failure. *In situ* XRD was employed to evaluate the time-dependent the evolution of surface byproducts on the Zn anode during deposition process (Figure 3j–l).[32] With the increase of deposition time, obvious peaks related to ZSH are detected on the Zn anode in LE and PAM, but not in MNPHE, which confirms the effective suppression of ZSH in MNPHE. In addition, the corrosion behaviors were further corroborated by Tafel curves. Notably, the MNPHE exhibits excellent corrosion resistance with a lower corrosion current (I_{corr} = 0.870 mA cm^{-2}) compared to LE (I_{corr} = 2.783 mA cm^{-2}) and PAM (I_{corr} = 1.556 mA cm^{-2}) (Figure 3m). Linear sweep voltammetry (LSV) curves show a lower hydrogen evolution onset potential of −99 mV than those of LE (−86 mV) and PAM (−78 mV), indicating suppressed electrochemical H_2O reduction (Figure S24). The inhibitory effect on parasitic reactions was further investigated by *in situ* electrochemical impedance spectroscopy tests. Zn anode/electrolyte interface in LE and PAM presents a trend of gradually increased interface impedance owing to the irregular Zn deposition and ZHS byproduct accumulations (Figure 3n,o). In contrast, the interfacial impedance at the Zn anode/electrolyte interface in the MNPHE gradually decreases during cycling (Figure 3p). Based on the above results, the confinement effect of free water molecules and anions in MNPHE positively regulates the growth behavior and corrosion resistance of Zn anode.

Based on the anode, we have further investigated the impact of multiconfinement effects on the cathode. The surface composition of the cycled Zn anode was analyzed by X-ray photoelectron spectroscopy (XPS) (Figure 4a). The migration of I_3^- is effectively suppressed in MNPHE, as evidenced by the absence of its characteristic peaks on the cycled Zn anode, in contrast to their clear presence in LE and PAM. Previous studies have demonstrated the anions confinement effect on SO_4^{2-} and Cl^- of MNPHE. The binding energy of I_3^--SBA-15 obtained through DFT calculations (−0.95 eV) is higher than that of I_3^--PAM (−0.52 eV) (Figure 4b), which suggests preferential coordination of I_3^- and SBA-15. In order to visualize the confinement effect of polyiodides in MNPHE, we systematically evaluated the blocking efficacy of various electrolytes against I_3^- migration using H-type electrolytic cells. As shown in Figure S25, the solution in the right chamber rapidly turns yellow with GF/D in LE. The solution gradually turns yellow after 20 min in PAM. In contrast, no color change is observed even after 40 min in MNPHE. Subsequent ultraviolet–visible spectroscopy (UV–vis) testing reveals distinct peaks corresponding to I_3^- in both LE and PAM, whereas no I_3^- peaks are detected in MNPHE. The MNPHE effectively suppresses the polyiodide shuttle effect, as evidenced by the characterizations and calculations above.

Beyond the shuttling effect of polyiodides, the hydrolysis of ICl is another critical factor affecting the reversible cycling of four-electron AZIBs. The hydrolysis mechanism of ICl proceeds via HIO intermediate formation, with proton dissociation from the hydrated ICl complex (ICl·HOH) serving as the rate-determining step ($ICl + H_2O \leftrightarrow ICl \cdot HOH \leftrightarrow HIO + H^+ + Cl^-$). Thermodynamic analysis confirms that the MNPHE presents a higher energy barrier (4.49 eV) for the hydrolysis reaction compared to the LE (3.27 eV) and PAM (2.01 eV) electrolytes (Figure 4c), which significantly impedes proton dissociation from the ICl-HOH intermediate, thereby inhibiting the hydrolysis of I^+. In order to elucidate the transformation of iodine species during electron transfer for four-electron AZIBs, we conducted UV–vis tests on cathodes at different potentials (0.6 → 1.8 → 0.6 V) (Figure 4d–f). In the MNPHE, the characteristic peak intensity of I^+ at 1.8 V is significantly stronger than those in LE and PAM, revealing complete conversion of I_2 to I^+. In contrast, the LE and PAM systems exhibit incomplete I^0/I^+ conversion along with prominent I_3^- characteristic peaks, indicating that the MNPHE can stabilize the I^+ while suppressing polyiodide formation. Thus, thermodynamic analysis via Gibbs free energy (ΔG) calculations was performed for iodine species interconversion in different electrolytes (Figure 4g). The reduction of I_2 to I_3^- is spontaneous and exothermic in LE and PAM electrolytes. However, in MNPHE, the conversion from $3*I_2$ to $2*I_3^-$ is hindered due to an unfavorable ΔG increase (+0.116 eV). Notably, a significant ΔG drop (−1.335 eV) between $3*I_2$ and $6*I^-$ indicates that I_2 can be directly reduced to I^-, avoiding the generation and accumulation of I_3^-.[33] Furthermore, the oxidation of I_2 to ICl is thermodynamically more favored in the MNPHE than in the LE and PAM electrolytes, suggesting that the $I^0 \rightarrow I^+$ reaction pathway is thereby accelerated. These results indicate that MNPHE more favorably suppresses ICl hydrolysis and I_3^- generation.

Leveraging these advantages, MNPHE exhibits markedly enhanced self-discharge performance. As shown in Figures 4h and S26–28, the CE of the Zn||I_2 cell with LE is only 6% after 24 h of resting. For PAM, the CE and voltage gradually diminish with prolongation of the resting time and the CE is almost zero when the resting time reaches 720 h. In contrast, the fully charged MNPHE system retains 80% of its capacity even after three months of storage, demonstrating significantly excellent self-discharge suppression ability. Although the discharge voltage platform decreases after standing for 720 and 2160 h, indicating that I^+ ions are consumed due to hydrolysis during the standing process, the high CE similar at 81% and 80%. This suggests that most of the capacity loss stems from the irreversible hydrolysis of I^+. While MNPHE offers advantages in suppressing I^+ hydrolysis compared to LE and PAM, further improvement is still needed in immobilizing I^+ over long periods. The self-discharge test is key evidence that MNPHE can inhibit the shuttling of polyiodide ions in Zn–I_2 batteries. Maintaining a high CE of 80% after three months of storage strongly proves that MNPHE can inhibit the formation and shuttling of I_3^-. Remarkly, our work stands out with the best self-discharge performance of four-electron AZIBs compared to the previous results, demonstrating promising potential for the practical applications (Figure 4i and Table S3).[34−42] The integrated experimental and theoretical analyses reveal that MNPHE effectively promotes iodine redox conversion, improves electrochemical reaction kinetics, and simultaneously mitigates polyiodide shuttle effects and I^+ hydrolysis (Figure 4j).

Due to the multiconfinement effects of MNPHE, the side reaction at the cathode and anode are effectively suppressed,

https://doi.org/10.1021/acsnano.5c20669
ACS Nano 2026, 20, 5217−5227

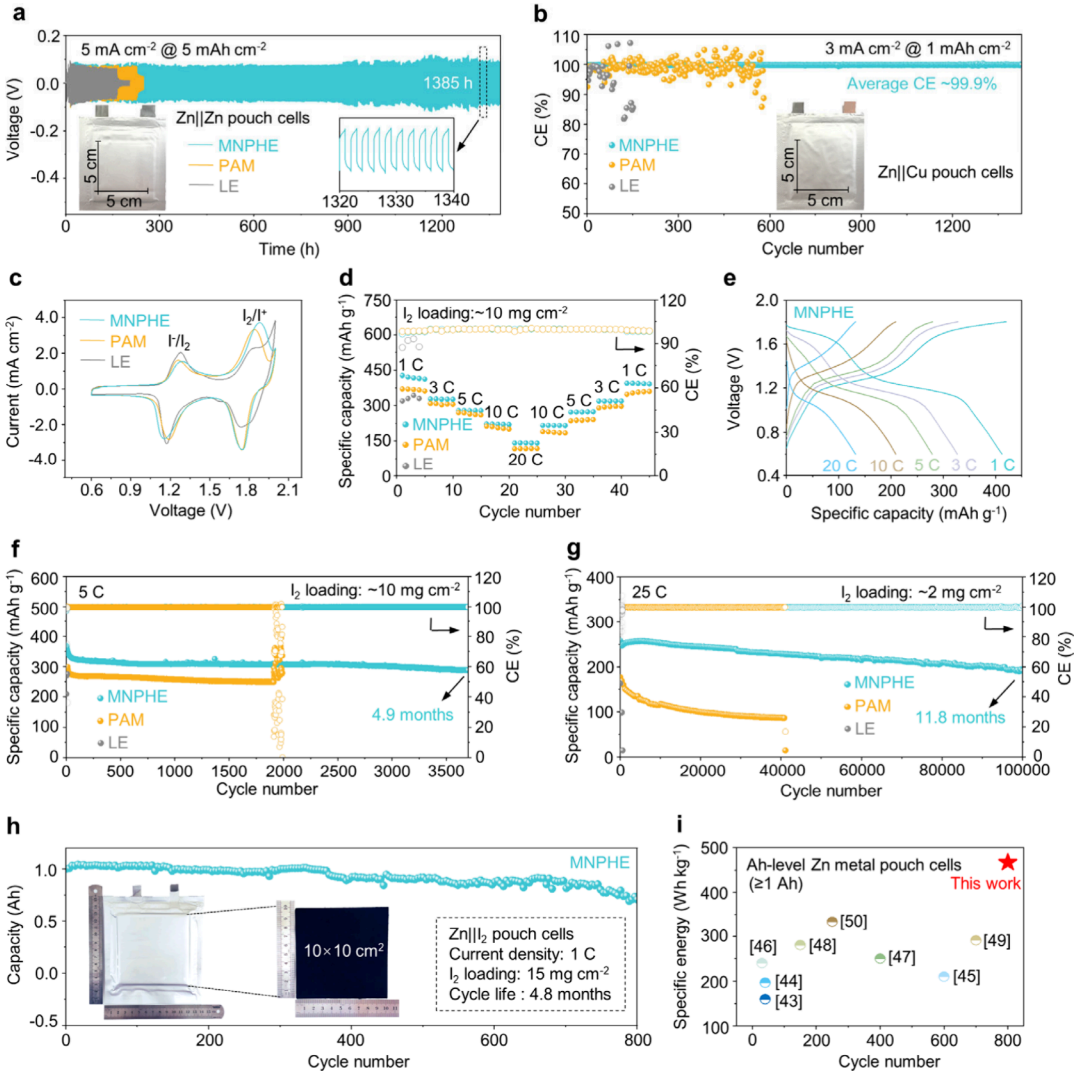

Figure 5. Electrochemical performance of half and full cells. (a) Cycling performance of Zn||Zn pouch cells with LE, PAM, and MNPHE electrolytes (inset: a digital photograph of the pouch cell). (b) Cycling and CE of Zn||Cu pouch cells. (c) CV profiles of full cells at 0.2 mV s^{-1}. (d) Rate performance of full cells at various current densities. (e) Charge/discharge profiles of full cells with MNPHE. Long-term cycling at (f) 1 and (g) 25 C. (h) Cycling performance of Zn||I_2 pouch cells using MNPHE at 1 C. (i) Comparison of the specific energy and cycle life of Ah-level Zn metal pouch cells (≥1 Ah) in this work and prior literature (based on the mass of cathode active materials).

enhancing cycling lifespan of the battery. Zn||Zn cells were used to evaluate the stability of the Zn anodes in different electrolytes. As shown in Figure S29, the electrochemical cycling stability of the 1.0 wt % MNPHE is optimal. This is because that high concentration of SBA-15 could block the transport of Zn^{2+}, and low concentration of SBA-15 results in undesirable anion confinement effect. The Zn||Zn cells with MNPHE exhibit excellent rate performance, even at 500 mA cm^{-2}. Nevertheless, the Zn||Zn cells with PAM and LE undergo short-circuiting at 300 and 200 mA cm^{-2}, respectively (Figure S30). Furthermore, the Zn||Zn cells with MNPHE exhibit optimal cycling performance under current densities of 10 and 20 mA cm^{-2} (Figure S31). To validate the practical applicability of MNPHE, we subsequently fabricated large-format (5 × 5 cm^2) symmetrical Zn||Zn pouch cells. As shown in Figure S32, Zn||Zn pouch cells with MNPHE attain a stable cycle life of more than 2000 h at 3 mA cm^{-2} and 3 mAh cm^{-2}, while those with PAM and LE fail due to short-circuit after merely 355 and 104 h, respectively. MNPHE exhibits a 1385 h lifespan at 5 mA cm^{-2} and 5 mAh cm^{-2}, outperforming PAM and LE in Zn||Zn pouch cells (Figure 5a). We further conduct tensile tests on the cycled PAM and MNPHE (Figure S33), and the MNPHE maintains superior mechanical properties (328 kPa tensile strength), whereas the PAM only withstand 23 kPa tensile strength. This demonstrates that the framework confinement effect can effectively mitigate the degradation of MNPHE caused by repeated Zn stripping/deposition processes, thereby enhancing the cycling stability of Zn||Zn cells. Then, we engineered Zn||Cu pouch cells with an electroactive area of 25 cm^2 for Zn plating/striping reversibility validation. As shown in Figure 5b, Zn||Cu cells with LE and PAM demonstrate rapid Coulombic efficiency (CE) fluctuation and degradation, sustaining merely 158 and 550 cycles, respectively. Strikingly, Zn||Cu pouch cells using MNPHE exhibit exceptional cyclability over 1400 cycles with a high average CE of 99.9%.

The basic redox differences of full cells with different electrolyte compositions were revealed by cyclic voltammetry (CV) (Figure 5c). LE and PAM based cells manifest confined I^-/I^0 and I^0/I^+ redox activity. In stark contrast, Zn||I_2 full cells

https://doi.org/10.1021/acsnano.5c20669
ACS Nano 2026, 20, 5217−5227

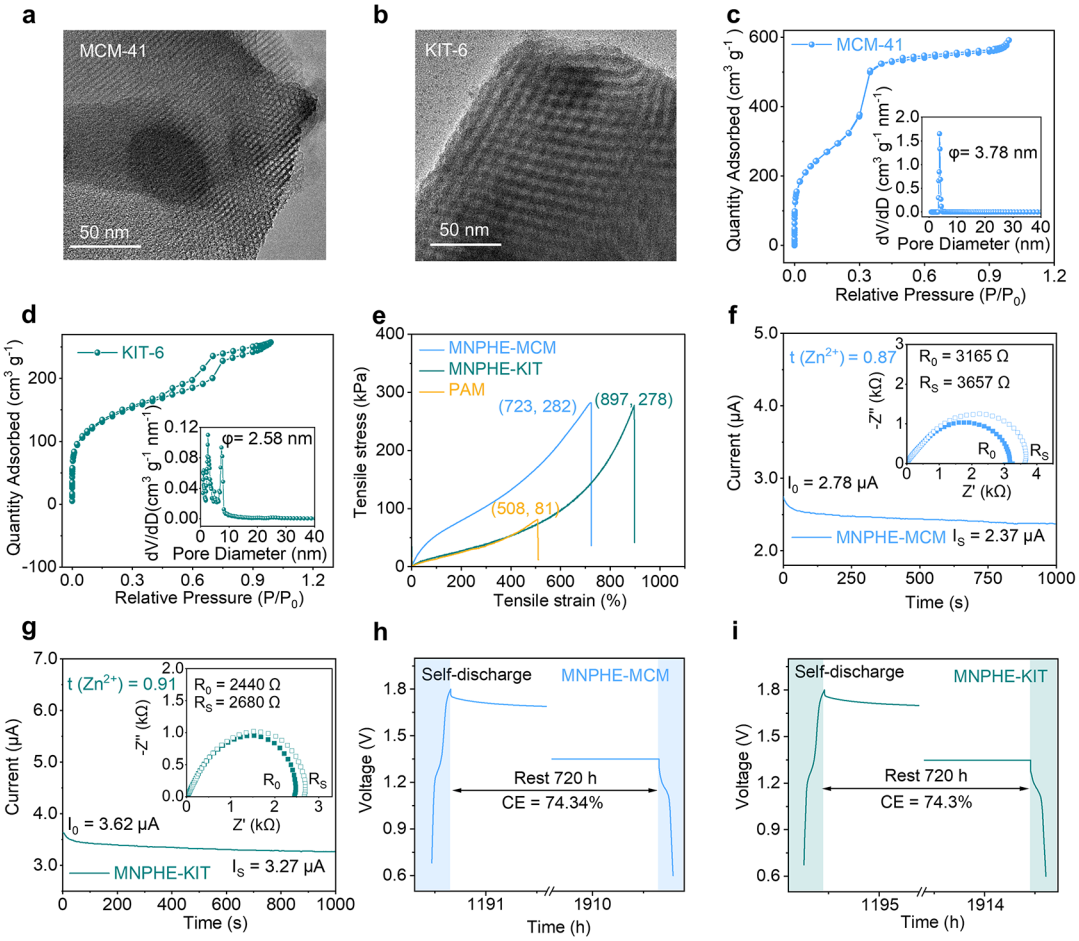

Figure 6. Expanded results of nanoconfined polymerization strategy. (a,b) TEM images and (c,d) nitrogen adsorption−desorption isotherms and pore size distributions of MCM-41 and KIT-6. (e) Tensile stress−stretch curves and (f,g) $t_{Zn^{2+}}$ of MNPHE-MCM and MNPHE-KIT. (h,i) Voltage−time profile of the Zn||I_2 cells with MNPHE-MCM and MNPHE-KIT after 720 h of resting.

with MNPHE exhibit synchronized dual-redox signatures of robust I^-/I^0 interconversion (1.15/1.29 V) coupled with intensified I^0/I^+ transitions (1.75/1.87 V), indicating faster redox kinetics. In exploring the practical development and application of AZIBs, it has been found that the mass loading of cathode materials is crucial for achieving high-energy-density batteries. Hence, the cycling performance of Zn||I_2 full cells is investigated under a high I_2 cathode loading of 10 mg cm^{-2}. Even at high current densities (from 1 to 20 C), the Zn||I_2 cell with MNPHE exhibits excellent rate performance. However, the substantial formation of I_3^- resulted in overcharging of the Zn||I_2 battery with LE after 5 cycles (Figure S34). Such outstanding rate performance indicates that MNPHE effectively suppresses the shuttle effect of I_3^- and enhances reaction kinetics, thereby significantly improving the capacity and reversibility of Zn||I_2 cells (Figure 5d). The corresponding charge−discharge curves of MNPHE-based Zn||I_2 cells also show two distinct plateaus, indicating the facilitated $I^-/I^0/I^+$ four-electron conversion (Figure 5e). Similarly, the rate performance of the Zn||I_2 battery under low loading (2 mg cm^{-2}) also exhibited the same trend (Figure S35).

Except for enhanced rate performance, Zn||I_2 full cells also exhibit excellent cycling stability. As shown in Figure S36, Zn||I_2 cells with MNPHE display stable cycling performance and markedly high discharge specific capacity at 1 C compared to those with LE and PAM. The Zn||I_2 cell with MNPHE shows excellent performance at 5 C, with a cycle life of 3700 cycles and a capacity of 287.8 mAh g^{-1} under 10 mg cm^{-2} I_2 loading (Figure 5f). Furthermore, the cycling stability of Zn||I_2 full cells is also evaluated at a high rate of 25 C with a low loading (2 mg cm^{-2}). The Zn||I_2 cells with MNPHE demonstrate a breakthrough cyclability of 100,000 cycles (11.8 months) and a CE of nearly 100% (Figure 5g), which demonstrates the longest lifespan among currently reported four-electron AZIBs (Table S4). To demonstrate the potential commercialization of the four-electron AZIBs, we fabricate a pouch cell using a layer-to-layer "sandwich" structure, which contains two stacks of Zn-MNPHE-I_2/I_2-MNPHE-Zn (Figure S37). As shown in Figure 5h, the cathode exhibits a length of 10 cm and width of 10 cm with an I_2 loading of 15 mg cm^{-2}. Owing to simultaneous electrochemical optimization of four-electron $I^-/I^0/I^+$ redox mediation and Zn anode stabilization by multiconfinement effects of MNPHE, the four-electron Zn||I_2 pouch cells utilizing MNPHE manifest a notable initial capacity of 1.0 Ah at 1 C and an exceptionally prolonged cycling life of 800 cycles. The calculated energy density (466.7 Wh kg^{-1}) and cycling stability surpass those of recently reported Ah-level aqueous Zn metal pouch cells (based on the mass of cathode active materials) (Figure 5i and Table S5),[43−50] indicating the promising feasibility of MNPHE in practical four-electron AZIBs. Four-electron conversion iodine cathodes offer significant advantages in energy density and

https://doi.org/10.1021/acsnano.5c20669
ACS Nano 2026, 20, 5217−5227

cycle life over other cathode materials, which reveals a critical breakthrough for implementing four-electron Zn||I_2 chemistry in grid-scale energy storage systems.

To elucidate the universality of the nanoconfined polymerization strategy, we selected MCM-41 and KIT-6 mesoporous nanomaterials with the same pore structure as SBA-15 (Figure 6a,b) for extension. The pore sizes of MCM-41 and KIT-6 are 3.775 and 2.582 nm, respectively (Figure 6c,d), both within the typical mesoporous range (2−50 nm). FTIR confirmed the presence of abundant Si−OH groups on MCM-41 and KIT-6, which is crucial for achieving the multiconfinement effects of the hydrogel electrolyte (Figure S38). Therefore, we successfully prepared hydrogel electrolytes with MCM-41 and KIT-6 (MNPHE-MCM and MNPHE-KIT) via a nanoconfined polymerization strategy. Mechanical tests on the hydrogel electrolytes showed that the stress−strain properties of MNPHE-MCM and MNPHE-KIT were significantly enhanced (Figure 6e). Benefiting from the anion confinement effect, the $t_{Zn^{2+}}$ values of MNPHE-MCM and MNPHE-KIT are 0.87 and 0.91, respectively, which are much higher than those of LE and PAM (Figure 6f,g and Table S6). In addition, Zn||I_2 cells with MNPHE-MCM and MNPHE-KIT also achieved better self-discharge performance, which is attributed to the multiconfinement effects (Figure 6h,i). Additionally, the Zn||Zn pouch cell also demonstrated a superior cycling performance at 5 mA cm^{-2} and 5 mAh cm^{-2} (Figure S39). These results validate that the hydrogel electrolyte, obtained via *in situ* polymerization within the nanochannels of mesoporous nanoparticles, effectively suppresses side reactions at both electrodes through a multiconfinement mechanism, thereby enhancing cycling stability. This work develops a universal strategy to design high-energy-density four-electron AZIBs.

CONCLUSIONS

In summary, the MNPHE prepared via a nanoconfined polymerization strategy can realize long-life and highly reversible Ah-level four-electron zinc−iodine pouch cells. The multiconfinement effects in MNPHE, including skeleton confinement, anion confinement, and free water confinement, simultaneously improve the mechanical strength and Zn^{2+} transfer number, enabling uniform Zn plating/stripping while effectively inhibiting the polyiodide shuttle effect and I^+ species hydrolysis, enhancing four-electron $I^-/I^0/I^+$ redox reversibility and kinetics under high mass loading of I_2 cathode. As a result, Zn||I_2 full cells exhibit a record-low self-discharge of 20% after three months of resting. An excellent cycling life of 100,000 cycles at high rate of 25 C is obtained for the Zn||I_2 cells. Most remarkably, MNPHE achieves a breakthrough of cycling performance in Ah-level four-electron Zn||I_2 pouch cells. This work emphasizes the universal viability of nanoconfined polymerized hydrogel electrolyte design strategy for achieving practical and long-life Ah-level four-electron zinc−iodine pouch cells, addressing critical challenges in high-energy aqueous battery design.

EXPERIMENTAL SECTION

Electrolyte Preparation

First, $ZnSO_4{\cdot}7H_2O$ (143.5 g) and $ZnCl_2$ (17.04 g) were dissolved in deionized water, then diluted to a final volume of 250 mL to prepare LE. Typically, AM (2 g) was first added into LE (10 mL) to form a transparent solution, followed by the addition of initiator APS solution (0.13 M, 400 μL) and cross-linker MBA solution (0.06 M, 400 μL); the presolution was dropped into a glass mold to complete free radical polymerization (FRP) at 80 °C and obtain the PAM. MNPHE was prepared through *in situ* polymerization of PAM within nanochannels of SBA-15 in LE. First, SBA-15 (6, 20, 60, and 100 mg) was dissolved in 10 mL of LE to prepare SBA-15 dispersion with different mass fractions of 0.3, 1.0, 3.0, and 5.0 wt % (based on AM), respectively (named 0.3 wt % MNPHE, 1.0 wt % MNPHE, 3.0 wt % MNPHE, and 5.0 wt % MNPHE). Subsequently, AM (2 g), initiator APS (0.13 M, 400 μL), and cross-linker MBA (0.06 M, 400 μL) were added successively. Finally, the hydrogel electrolytes were prepared via FRP. Additionally, two different mesoporous nanoparticles were selected: MCM-41 and KIT-6. The corresponding hydrogel electrolytes were also prepared using a similar process and were named MNPHE-MCM and MNPHE-KIT, respectively.

Electrode Preparation

The KB@I_2 composite cathode was fabricated by using a melt-diffused method. KB and I_2 (mass ratio 1:1) were mixed and hand-ground for 30 min. The mixture was then sealed in a Teflon-lined autoclave and heated at 80 °C for 6 h to prepare the KB&I_2 composite cathode. For the preparation of KB&I_2 electrodes, the KB&I_2 composite cathode was combined with KB and PTFE binder (7:2:1). The active material is finally pressed onto the Ti mesh. In the cathode of Zn||I_2 coin cells, the mass loading of I_2 is controlled at 2 or 10.0 mg cm^{-2}.

ASSOCIATED CONTENT

Supporting Information

The Supporting Information is available free of charge at https://pubs.acs.org/doi/10.1021/acsnano.5c20669.

Additional experimental procedures, calculation details, material characterization, electrochemical data, and theoretical calculations (PDF)

AUTHOR INFORMATION

Corresponding Authors

Dongdong Wang − *Power Battery & Systems Research Center, State Key Laboratory of Catalysis, Dalian Institute of Chemical Physics, Chinese Academy of Sciences, Dalian 116023, P. R. China*; Email: dongdongwang@dicp.ac.cn

Dan Luo − *Power Battery & Systems Research Center, State Key Laboratory of Catalysis, Dalian Institute of Chemical Physics, Chinese Academy of Sciences, Dalian 116023, P. R. China*; Email: luodan@dicp.ac.cn

Ming Feng − *Jilin Key Laboratory of Solid-State Laser Technology and Application, School of Physics, Changchun University of Science and Technology, Changchun 130022, P. R. China; Key Laboratory of Functional Materials Physics and Chemistry of the Ministry of Education, Jilin Normal University, Changchun 130103, P. R. China*; orcid.org/0000-0001-5921-0190; Email: mingfeng@jlnu.edu.cn

Zhongwei Chen − *Power Battery & Systems Research Center, State Key Laboratory of Catalysis, Dalian Institute of Chemical Physics, Chinese Academy of Sciences, Dalian 116023, P. R. China*; orcid.org/0000-0003-3463-5509; Email: zwchen@dicp.ac.cn

Authors

Renming Liu − *Power Battery & Systems Research Center, State Key Laboratory of Catalysis, Dalian Institute of Chemical Physics, Chinese Academy of Sciences, Dalian 116023, P. R. China; Jilin Key Laboratory of Solid-State Laser Technology and Application, School of Physics, Changchun University of Science and Technology, Changchun*

https://doi.org/10.1021/acsnano.5c20669
ACS Nano 2026, 20, 5217−5227

130022, P. R. China; Key Laboratory of Functional Materials Physics and Chemistry of the Ministry of Education, Jilin Normal University, Changchun 130103, P. R. China

Ze Gao − *Key Laboratory of Functional Materials Physics and Chemistry of the Ministry of Education, Jilin Normal University, Changchun 130103, P. R. China*

Daming Yang − *Key Laboratory of Functional Materials Physics and Chemistry of the Ministry of Education, Jilin Normal University, Changchun 130103, P. R. China*

Yuying Li − *Power Battery & Systems Research Center, State Key Laboratory of Catalysis, Dalian Institute of Chemical Physics, Chinese Academy of Sciences, Dalian 116023, P. R. China*

Xintao Long − *Power Battery & Systems Research Center, State Key Laboratory of Catalysis, Dalian Institute of Chemical Physics, Chinese Academy of Sciences, Dalian 116023, P. R. China*

Complete contact information is available at: https://pubs.acs.org/10.1021/acsnano.5c20669

Notes

The authors declare no competing financial interest.

■ ACKNOWLEDGMENTS

This work was supported by the Strategic Priority Research Program of the Chinese Academy of Sciences (XDB0600400), the Science and Technology Major Project of Liaoning Province (2024JH1/11700013), DICP Innovation Funding (DICP-I202433), the National Natural Science Foundation of China (52471229), and the Program for the Development of Science and Technology of Jilin Province (20250205055GH).

■ REFERENCES

(1) Gourley, S. W. D.; Brown, R.; Adams, B. D.; Higgins, D. Zinc-Ion Batteries for Stationary Energy Storage. *Joule* **2023**, *7*, 1415−1436.

(2) Liang, Y.; Dong, H.; Aurbach, D.; Yao, Y. Current Status and Future Directions of Multivalent Metal-Ion Batteries. *Nat. Energy* **2020**, *5*, 646−656.

(3) Liu, X. C.; Wei, X. L.; Zhang, Z.; Wang, X.; Liu, G. H.; Luo, D.; Li, J. D. Design of Defect-Rich MgCo-Layered Double Hydroxide Microspheres as Highly Effective Sulfur Reduction Reaction Electrocatalyst for High-Performance Li-S Batteries. *Renewables* **2024**, *2*, 162−170.

(4) Cao, Y. N.; Ju, S. D.; Zhang, Q.; Gao, K.; Marcelli, A.; Zhang, Z. P. Recent Progress in Aqueous Zinc-Ion Batteries Based on Conversion-Type Cathodes. *Adv. Powder Mater.* **2025**, *4*, No. 100278.

(5) Zhong, W.; Cheng, H.; Zhang, S. C.; Li, L. X.; Tan, C. Q.; Chen, W.; Lu, Y. Y. Cation-Driven Phase Transition and Anion-Enhanced Kinetics for High Energy Efficiency Zinc-Interhalide Complex Batteries. *Nat. Commun.* **2025**, *16*, 4586.

(6) Wu, Y. W.; Li, Y. Q.; Xie, M. H.; Chen, Z. H.; Wang, W. L.; Zheng, Z. J.; Yang, C. P.; Guo, Z. G. Desert Beetle-Inspired Hybrid Interphase Enables Extended Calendar Life of Aqueous Zinc Metal Batteries. *J. Colloid Interface Sci.* **2026**, *703*, No. 139063.

(7) Yan, Z. H.; Xu, L. B.; Zhu, H. Y. Advances in Electrocatalytic Semi-Hydrogenation of Acetylene in Aqueous Electrolyte: Progress, Challenges, and Opportunities. *Renewables* **2023**, *1*, 278−293.

(8) Wang, C. G.; Ji, X. X.; Liang, J. N.; Zhao, S. S.; Zhang, X. X.; Qu, G. M.; Shao, W. F.; Li, C. L.; Zhao, G.; Xu, X. J.; Li, H. Q. Activating and Stabilizing a Reversible Four Electron Redox Reaction of I^-/I^+ for Aqueous Zn-Iodine Battery. *Angew. Chem., Int. Ed.* **2024**, *63*, No. e202403187.

(9) Guan, D. Y.; Deng, Z. H.; Luo, W.; Cheng, C. J.; Wang, F. Y.; Cai, H. W.; Chen, R. X.; Wang, P.; Wu, M. Y.; Han, C. J.; Liu, Z. Y.; Ma, D. L.; Mai, L. Q. π-d Conjugated Coordination Mediated Catalysis for Four-Electron-Transfer Fast-Charging Aqueous Zinc-Iodine Batteries. *Matter* **2025**, *8*, No. 101932.

(10) Liu, T. T.; Lei, C. J.; Wang, H. J.; Xu, C.; Ma, W. J.; He, X.; Liang, X. Practical Four-Electron Zinc-Iodine Aqueous Batteries Enabled by Orbital Hybridization Induced Adsorption-Catalysis. *Sci. Bull.* **2024**, *69*, 1674−1685.

(11) Ke, J. Q.; Bai, K.; Zhang, Z. C.; Wen, Z. P.; Bu, J. S.; Tang, Y. C.; Liu, X. Q.; Ye, M. H.; Zhang, Y. F.; Li, C. C. Enabling I_3^-/I_2 Redox Couple toward High-Voltage Zn-Polyiodide Batteries by the Iodide-π Conjugation Effect. *ACS Nano* **2025**, *19*, 17746−17759.

(12) Yang, X.; Xie, M. H.; Yan, Z. J.; Ruan, H.; Yang, C. P.; Guo, Z. P.; Zheng, Z. J. High-Iodine-Loading Quasi-Solid-State Zinc-Iodine Batteries Enabled by a Continuous Ion-Transport Network. *Energy Environ. Sci.* **2025**, *18*, 4730−4739.

(13) Zhang, S. J.; Hao, J. N.; Wu, H.; Chen, Q. R.; Hu, Y. Y.; Zhao, X.; Qiao, S. S. Coordination Chemistry toward Advanced Zn-I_2 Batteries with Four-Electron $I^-/I^0/I^+$ Conversion. *J. Am. Chem. Soc.* **2025**, *147*, 16350−16361.

(14) Zong, W.; Li, J. T.; Zhang, C. Y.; Dai, Y. H.; Ouyang, Y.; Zhang, L. Q.; Li, J. W.; Zhang, W.; Chen, R. W.; Dong, H. B.; Gao, X.; Zhu, J. X.; Parkin, I. P.; Shearing, P.; Lai, F. L.; Amine, K.; Liu, T. X.; He, G. J. Dynamical Janus Interface Design for Reversible and Fast-Charging Zinc-Iodine Battery under Extreme Operating Conditions. *J. Am. Chem. Soc.* **2024**, *146*, 21377−21388.

(15) Wang, H. R.; Wei, W.; Liu, X. X.; Xu, S. C.; Dong, Y. F.; He, R. H. Ultrahigh-Capacity Epitaxial Deposition of Planar Zn Flakes Enabled by Amino-Rich Adhesive Hydrogel Electrolytes for Durable Low-Temperature Zinc Batteries. *Energy Storage Mater.* **2023**, *55*, 597−605.

(16) Liu, Z. P.; Hu, Y. F.; Lu, X.; Mo, Z. W.; Chen, G. M.; Liu, Z. X. Electrolyte Engineering of Quasi-solid-state Thermocells for Low-grade Heat Harvest at Sub-zero Temperatures. *Adv. Energy Mater.* **2024**, *14*, No. 2402226.

(17) Zhou, J.; Li, Q. Y.; Hu, X. M.; Wei, W. F.; Ji, X. B.; Kuang, G. C.; Zhou, L. J.; Chen, L. B.; Chen, Y. J. Water Molecules Regulation for Reversible Zn Anode in Aqueous Zinc Ion Battery: Mini-Review. *Chin. Chem. Lett.* **2024**, *35*, No. 109143.

(18) Guo, S. J.; Yan, M. Y.; Xu, D. M.; He, P.; Yan, K. J.; Zhu, J. X.; Yu, Y. K.; Peng, Z. Y.; Luo, Y. Z.; Cao, F. F. Anti-Freezing Hydrogel Electrolyte with a Regulated Hydrogen Bond Network Enables High-Rate and Long Cycling Zinc Batteries. *Energy Environ. Sci.* **2025**, *18*, 418−429.

(19) Zeng, X. X.; Zhang, S.; Long, T.; Zhao, Q. Y.; Wang, H. R.; Ling, W.; Wu, X. W.; Yu, A. P.; Chen, Z. W. An Amphipathic Ionic Sieve Membrane for Durable and Dendrite-Free Zinc-Ion Batteries. *Renewables* **2024**, *2*, 52−60.

(20) Wang, D. K.; Zhao, D. Y.; Chang, L.; Zhang, Y.; Wang, W. Y.; Zhang, W. M.; Zhu, Q. C. Interface Engineering of Electron-Ion Dual Transmission Channels for Ultra-Long Lifespan Quasi-Solid Zinc-Ion Batteries. *Energy Storage Mater.* **2025**, *74*, No. 103903.

(21) Tian, H.; Yao, M.; Guo, Y.; Wang, Z. Y.; Xu, D. H.; Pan, W.; Zhang, Q. Y. Hydrogel Electrolyte with Regulated Water Activity and Hydrogen Bond Network for Ultra-stable Zinc Electrode. *Adv. Energy Mater.* **2025**, *15*, No. 2403683.

(22) Chen, J. Z.; Chen, M. F.; Chen, H. L.; Yang, M.; Han, X.; Ma, D. T.; Zhang, P. X.; Wong, C. P. Wood-Inspired Anisotropic Hydrogel Electrolyte with Large Modulus and Low Tortuosity Realizing Durable Dendrite-Free Zinc-Ion Batteries. *Proc. Natl. Acad. Sci. U.S.A.* **2024**, *121*, No. e2322944121.

(23) Wang, F. F.; Zhang, J. P.; Lu, H. T.; Zhu, H. B.; Chen, Z. H.; Wang, L.; Yu, J. Y.; You, C. H.; Li, W. H.; Song, J. W.; Weng, Z.; Yang, C. P.; Yang, Q. H. Production of Gas-Releasing Electrolyte-Replenishing Ah-Scale Zinc Metal Pouch Cells with Aqueous Gel Electrolyte. *Nat. Commun.* **2023**, *14*, 4211.

(24) Cui, Y. L. S.; Chen, W. P.; Xin, W. W.; Ling, H. Y.; Hu, Y. H.; Zhang, Z. H.; He, X. F.; Zhao, Y.; Kong, X. Y.; Wen, L. P.; Jiang, L.

Gradient Quasi-solid Electrolyte Enables Selective and Fast Ion Transport for Robust Aqueous Zinc-ion Batteries. *Adv. Mater.* **2024**, *36*, No. 2308639.
(25) Li, G. J.; Zhao, Z. H.; Zhang, S. L.; Sun, L.; Li, M. N.; Yuwono, J. A.; Mao, J. F.; Hao, J. N.; Vongsvivut, J.; Xing, L. D.; Zhao, C. X.; Guo, Z. P. A Biocompatible Electrolyte Enables Highly Reversible Zn Anode for Zinc Ion Battery. *Nat. Commun.* **2023**, *14*, 6526.
(26) Du, Z. H.; Shen, S. T.; Su, X. Z.; Zhuang, Y. H.; Chen, M. X.; Zhang, X. Y.; Lin, Z. P.; Yu, L.; Zhou, P. P.; Wu, M. M.; Lyu, X. L.; Zou, Z. G. A Robust and Tough Composite Hydrogel Electrolyte with Anion-locked Supramolecular Network for Zinc Ion Batteries. *Adv. Mater.* **2025**, *37*, No. 2502328.
(27) Yao, L. B.; Liu, J. H.; Zhang, F. F.; Wen, B.; Chi, X. W.; Liu, Y. Reconstruction of Zinc-Metal Battery Solvation Structures Operating from −50 ∼ + 100 °C. *Nat. Commun.* **2024**, *15*, 6249.
(28) Sun, M.; Ji, G. C.; Li, M. Z.; Zheng, J. P. A Robust Hydrogel Electrolyte with Ultrahigh Ion Transference Number Derived from Zincophilic "Chain-gear" Network Structure for Dendrite-free Aqueous Zinc Ion Battery. *Adv. Funct. Mater.* **2024**, *34*, No. 2402004.
(29) Xia, H.; Xu, G.; Cao, X.; Miao, C. Y.; Zhang, H. N.; Chen, P. Y.; Zhou, Y.; Zhang, W.; Sun, Z. M. Single-Ion-Conducting Hydrogel Electrolytes Based on Slide-Ring Pseudo-Polyrotaxane for Ultralong-Cycling Flexible Zinc-Ion Batteries. *Adv. Mater.* **2023**, *35*, No. 2301996.
(30) Wang, R.; Zhu, J. C.; Yang, M.; Niu, Z. Q. Simultaneous Manipulation of Anions and Water Molecules by Lewis Acid-Base for Highly Stable Zn Anodes. *Angew. Chem., Int. Ed.* **2025**, *64*, No. e202501327.
(31) Deng, R. Y.; Chen, J. H. Y.; Chu, F. L.; Qian, M. Z.; He, Z. J.; Robertson, A. W.; Maier, J.; Wu, F. X. Soggy-sand" Chemistry for High-voltage Aqueous Zinc-ion Batteries. *Adv. Mater.* **2024**, *36*, No. 2311153.
(32) Wu, J. H.; Cai, H. W.; Deng, Z. H.; Gaumet, J. J.; Bao, Y.; Luo, W. Application of In-situ Characterization Techniques in Modern Aqueous Batteries. *Rare Met.* **2024**, *43*, 3553−3575.
(33) Yang, Y. Q.; Liang, S. Q.; Lu, B. G.; Zhou, J. Eutectic Electrolyte Based on *N*-Methylacetamide for Highly Reversible Zinc-Iodine Battery. *Energy Environ. Sci.* **2022**, *15*, 1192−1200.
(34) Jiang, P. J.; Du, Q. J.; Lei, C. J.; Xu, C.; Liu, T. T.; He, X.; Liang, X. Stabilized Four-Electron Aqueous Zinc-Iodine Batteries by Quaternary Ammonium Complexation. *Chem. Sci.* **2024**, *15*, 3357−3364.
(35) Du, W. Y.; Miao, L.; Song, Z. Y.; Zheng, X. W.; Hu, C. M.; Lv, Y. K.; Gan, L. H.; Liu, M. X. Organic Iodine Electrolyte Starting Triple I^+ Storage in In-Based Metal-Organic Frameworks for High-Capacity Aqueous Zn-I_2 Batteries. *Chem. Eng. J.* **2024**, *484*, No. 149535.
(36) Zou, Y. P.; Liu, T. T.; Du, Q. J.; Li, Y. Y.; Yi, H. B.; Zhou, X.; Li, Z. X.; Gao, L. J.; Zhang, L.; Liang, X. A Four-Electron Zn-I_2 Aqueous Battery Enabled by Reversible $I^-/I_2/I^+$ Conversion. *Nat. Commun.* **2021**, *12*, 170.
(37) Liang, G. J.; Liang, B. C.; Chen, A.; Zhu, J. X.; Li, Q.; Huang, Z. D.; Li, X. L.; Wang, Y.; Wang, X. Q.; Xiong, B.; Jin, X.; Bai, S. C.; Fan, J.; Zhi, C. Y. Development of Rechargeable High-Energy Hybrid Zinc-Iodine Aqueous Batteries Exploiting Reversible Chlorine-Based Redox Reaction. *Nat. Commun.* **2023**, *14*, 1856.
(38) Liu, T. T.; Lei, C. J.; Wang, H. J. Y.; Li, J. Y.; Jiang, P. J.; He, X.; Liang, X. Aqueous Electrolyte with Weak Hydrogen Bonds for Four-electron Zinc-Iodine Battery Operates in a Wide Temperature Range. *Adv. Mater.* **2024**, *36*, No. 2405473.
(39) Li, W. D.; Xu, H. Y.; Zhang, H. Y.; Wei, F. C.; Zhang, T. T.; Wu, Y.; Huang, L. Y.; Fu, J. W.; Jing, C. B.; Cheng, J. G.; Liu, S. H. Designing Ternary Hydrated Eutectic Electrolyte Capable of Four-Electron Conversion for Advanced Zn-I_2 Full Batteries. *Energy Environ. Sci.* **2023**, *16*, 4502−4510.
(40) Chen, M. H.; Chen, G. H.; Sun, C. X.; Li, X. Y.; Zhang, M. H.; Hua, H. M.; Zhao, J. B.; Yang, Y. SiO_2 Nanoparticles-induced Antifreezing Hydrogel Electrolyte Enables Zn-I_2 Batteries with Complete and Reversible Four-electron-transfer Mechanisms at Low Temperatures. *Angew. Chem.* **2025**, *64*, No. e202502005.
(41) Liu, L.; Zhang, L. H.; Liu, Y. Y.; Zhang, S. L.; Wang, R.; Li, F. J.; Li, H. B.; Hao, J. N.; Zhang, C. F.; Guo, Z. P. Enhanced Redox Kinetics of Aqueous $I^-/I_2/I^+$ Conversion Chemistry in Hydrated Eutectic Electrolyte over a Wide Temperature Range. *Adv. Energy Mater.* **2025**, *15*, No. 2501460.
(42) Zhu, J. B.; Zhang, S. H.; Ni, J. F.; Li, L. Interhalogen and the Salting-out Effect Enable High-Capacity and Long-Cycle Zn//I_2 Aqueous Microbatteries. *Matter* **2025**, *8*, No. 102104.
(43) Guo, S.; Qin, L. P.; Wu, J.; Liu, Z. X.; Huang, Y. H.; Xie, Y. M.; Fang, G. Z.; Liang, S. L. Conversion-Type Anode Chemistry with Interfacial Compatibility toward Ah-Level near-Neutral High-Voltage Zinc Ion Batteries. *Natl. Sci. Re.* **2024**, *11*, No. nwae181.
(44) Xu, Z. W.; Li, J. P.; Fu, Y. F.; Ba, J. J.; Duan, F. X.; Wei, Y. J.; Wang, C. Z.; Zhao, K. N.; Wang, Y. Z. Suppression of Interfacial Water Layer with Solid Contact Using an Ultrathin, Water-Repellent, and Zn^{2+}-Selective Layer for Ah-Level Zinc Metal Batteries. *Energy Environ. Sci.* **2025**, *18*, 4251−4261.
(45) Gan, H.; Li, H.; Xu, M. W.; Han, C. P.; Cheng, H. M. Failure Mechanisms and Remedy of an Ultrathin Zn Metal Anode in Pouch Cells. *Joule* **2024**, *8*, 3054−3071.
(46) Fu, Y. F.; Li, J. P.; Wu, M. Q.; Ba, J. J.; Zhang, J.; Zhao, Y. S.; Wei, Y. J.; Zhao, K. M.; Wang, Y. Z. Selective Masking of Active Sites in Zinc Metal via Galvanic Replacement Reaction for Highly Reversible Ah-level Zinc-I_2 Batteries. *Angew. Chem., Int. Ed.* **2025**, *64*, No. e202500731.
(47) Wang, Y.; Wang, T. R.; Bu, S. Y.; Zhu, J. X.; Wang, Y. B.; Zhang, R.; Hong, H.; Zhang, W. J.; Fan, J.; Zhi, C. Y. Sulfolane-Containing Aqueous Electrolyte Solutions for Producing Efficient Ampere-Hour-Level Zinc Metal Battery Pouch Cells. *Nat. Commun.* **2023**, *14*, 1828.
(48) Lv, W. S.; Tan, Y.; Guo, C. Y.; He, X.; Zeng, L. X.; Zhu, J. L.; Yang, L.; Chen, Z. J.; Yin, X. C.; Xu, J.; He, H. B. Triple Regulation of Water Molecules Behavior to Realize High Stability and Broad Temperature Tolerance in Aqueous Zinc Metal Batteries via a Novel Cost-Effective Eutectic Electrolyte. *Adv. Energy Mater.* **2025**, *15*, No. 2403689.
(49) Wang, L. P.; Zhang, B.; Zhou, W. H.; Li, H. P.; Dong, H. B.; Jin, H. R.; Yang, Z. F.; Li, W.; Zhao, Z. W.; Zhao, D. Y.; Chao, D. L. Cation-in-mesopore Complex for 20 Ah-level Aqueous Battery. *Angew. Chem., Int. Ed.* **2025**, *64*, No. e202501010.
(50) Hu, X. Y.; Dong, H. B.; Gao, N.; Wang, T. L.; He, H. Z.; Gao, X.; Dai, Y. H.; Liu, Y. Y.; Brett, D. J. L.; Parkin, I. P.; He, G. J. Self-Assembled Polyelectrolytes with Ion-Separation Accelerating Channels for Highly Stable Zn-Ion Batteries. *Nat. Commun.* **2025**, *16*, 2316.

https://doi.org/10.1021/acsnano.5c20669
ACS Nano 2026, 20, 5217−5227